

The Tianlai dish array low-z surveys forecasts

Olivier Perdereau^{1*}, Réza Ansari¹, Albert Stebbins⁴, Peter T. Timbie²,
 Xuelei Chen^{3,5,6}, Fengquan Wu³, Jixia Li^{3,5}, John P. Marriner⁴,
 Gregory S. Tucker¹², Zhiping Chen⁸, Yanping Cong^{3,5}, Santanu Das²,
 Qizhi Huang^{3,5}, Yichao Li⁹, Tao Liu⁸, Yingfeng Liu^{3,5}, Christophe Magneville¹⁴,
 Chenhui Niu³, Calvin Osinga², Trevor M. Osholm², Jeffrey B. Peterson¹⁰, Anh Phan²,
 Huli Shi³, Gage Siebert², Shijie Sun^{3,5}, Haijun Tian¹¹, Qunxiong Wang¹¹,
 Rongli Wang⁸, Yougang Wang³, Yanlin Wu⁶, Yidong Xu³, Kaifeng Yu^{3,5},
 Zijie Yu^{3,5}, Jiao Zhang¹³, Juyong Zhang⁸, Jialu Zhu⁸, Shifan Zuo^{3,5,6}

¹*IJCLab, University of Paris-Saclay, CNRS/IN2P3, Université Paris-Saclay, Orsay, France*

²*Department of Physics, University of Wisconsin Madison, 1150 University Ave, Madison WI 53703, USA*

³*National Astronomical Observatory, Chinese Academy of Science, 20A Datun Road, Beijing 100101, P. R. China*

⁴*Fermi National Accelerator Laboratory, P.O. Box 500, Batavia IL 60510-5011, USA*

⁵*University of Chinese Academy of Sciences Beijing 100049, P. R. China*

⁶*Center of High Energy Physics, Peking University, Beijing 100871, P. R. China*

⁷*Department of Astronomy and Tsinghua Center for Astrophysics, Tsinghua University, Beijing 100084, P.R.China*

⁸*Hangzhou Dianzi University, 115 Wenyi Rd., Hangzhou 310018, P. R. China*

⁹*College of Sciences, Northeastern University, Shenyang Liaoning, P. R. China.*

¹⁰*Department of Physics, Carnegie Mellon University, 5000 Forbes Avenue, Pittsburgh, PA 15213, USA*

¹¹*China Three Gorges University, Yichang 443002, P. R. China*

¹²*Department of Physics, Brown University, 182 Hope St., Providence, RI 02912, USA*

¹³*College of Physics and Electronic Engineering, Shanxi University, Taiyuan, Shanxi 030006, P. R. China*

¹⁴*CEA, DSM/IRFU, Centre d'Etudes de Saclay, 91191 Gif-sur-Yvette, France*

Accepted XXX. Received YYY; in original form ZZZ

ABSTRACT

We present the science case of the surveys planned for the Tianlai dish array interferometer, covering the very low redshift range $z \lesssim 0.1$ by tuning the instrument analog electronic system to low frequencies, covering the [1300, 1400] MHz range. A realistic simulation of the survey, starting from generation of mock visibility data according to the survey strategy, then map reconstruction followed by a simple foreground subtraction has been performed. We show that a rather deep survey toward the North Celestial Pole (NCP), covering an area of $\sim 100\text{deg}^2$ over a year, would reach a sensitivity a few mK, and would be marginally impacted by the mode-mixing given the interferometer configuration. Tianlai would then be able to detect closeby, massive H_I clumps, as well as clear cross-correlation signal at x-sigma with NCCS optical galaxies. We have also studied the performance of a mid-latitude survey, covering several thousand degrees, overlapping SDSS main survey footprint. Despite a higher noise level as well as significant distortions due to mode mixing, Tianlai would be able to detect the cross-correlation of the 21cm intensity mapping signal with the SDSS low-z spectroscopic galaxy sample. Thanks to these signals within reach, it would be possible to assess precisely the impact of instrument and survey imperfection, such as calibration uncertainties, lack of precise beam knowledge and correlated noise on survey sensitivity and mode mixing.

Key words: galaxies: evolution – large-scale structure – 21-cm

1 INTRODUCTION

21cm Intensity Mapping is a promising technic to map the cosmological large scale matter distribution through the ob-

* E-mail: olivier.perdereau@ijclab.in2p3.fr

ervation of 21cm radio emission/absorption of neutral hydrogen gas (H_I), without detection of individual sources (see e.g. (Bharadwaj et al. 2001; Battye et al. 2004)) and has been largely explored in the context of the search for EoR (Epoch of Reionisation) signal (see (Pritchard & Loeb 2008; Morales & Wyithe 2010) for example). Subsequently, it was suggested that 21cm Intensity Mapping surveys could be used to constrain Dark Energy through the measurement of the BAO scale ((Chang et al. 2008; Seo et al. 2010; Ansari et al. 2012)). These surveys require instruments with large instantaneous bandwidth and field of view and several groups have built dense interferometric arrays to explore IM, such as CHIME (Bandura et al. 2014) or Tianlai (Chen 2012) in the last decade. Smaller instruments such as PAON4 (Ansari et al. 2020) or BMX (O'Connor et al. 2020) have also been built to explore specific technical aspects of these arrays, as well as transit mode operation and calibration. CHIME has proved to be a powerful radio burst and pulsar observation machine (The CHIME/FRB Collaboration et al. 2021) and has motivated the design and construction of larger, dish-based, dense interferometric arrays, HIRAX (Newburgh et al. 2016) and CHORD (Vanderlinde et al. 2019). **Should we mention HERA, LOFAR, MWA ... ?**

Tianlai is an international collaboration led by NAOC which has built and operates two radio-interferometers dedicated to the 21cm Intensity Mapping since 2015 (Das et al. 2018). A first instrument is composed of three cylindrical reflectors, equipped with a total of 96 dual polarisation feeds (Li et al. 2020) while the second instrument, the Tianlai Dish Pathfinder Array features 16, 6 meter diameter on-axis dishes, equipped with dual polarisation feeds, and arranged in a near hexagonal configuration. The two instruments are located in a radio quiet site in Hongliuxia, Balikun county, in the Xinjiang autonomous region, in north-west China. The two arrays have been observing in the frequency band [700, 800] MHz, corresponding to the redshift range $z \sim [0.775, 1.029]$ and we recently reported on the various aspects of the operation and performances of the Tianlai Dish Pathfinder Array (Wu et al. 2021).

Detection of cosmological H_I signal and the science reach of large instruments to constrain cosmological model and the dark energy equation of state through IM surveys covering the redshift range $z \lesssim 3 - 6$ has been extensively explored for large dedicated instruments (e.g. (Bull et al. 2015), (Cosmic Visions 21 cm Collaboration et al. 2018),) or with SKA (Villaescusa-Navarro et al. 2017) or FAST (Smoot & Debono 2017).

However, the two Tianlai pathfinder instruments, specially the Dish array are too small to be sensitive to the cosmological 21cm signal around $z \sim 1$. In this paper, we study the extragalactic H_I signals that could be detected by the Tianlai Dish Array by tuning its frequency band to the very low redshift $z \lesssim 0.1$, through a detailed simulation of the reconstructed signal, taking into account the instrument response and survey strategy. Such an H_I signal within reach of the instrument would make it possible to assess precisely the instrument and data analysis performance regarding key issues such as gain, phase and band pass calibration, impact of instrument noise, beam and array configuration knowledge on the reconstructed 3D maps and level of residuals after foreground subtraction.

We present an overview of the science targets of the

Tianlai Dish Array low-redshift surveys in section 2, while the simulation and analysis method common to the different science cases are discussed in section 3, as well the expected survey sensitivities. Possible direct detection of nearby H_I clumps or galaxies is presented in section 4, and the prospects of detecting the Large Scale structures at low redshifts ($z \lesssim 0.1$) in cross correlation with the SDSS and NCCS optical galaxy surveys is discussed in section 5. Our findings are summarised and further discussed in the last section 6.

left from the initial plan - remove once done

- HI intensity mapping
- Tianlai project, reference to the cylinder paper and dish array paper
- Reminding the main challenges : reaching the sensitivity through long integration time, amplitude and phase calibration when observing in transit, and separating the cosmological 21cm signal from the foregrounds : references, focus on the high-k analysis

The usual description of the paper structure

- Science reach of Tianlai dish array surveys, at low ($z \sim 0.1$) and medium ($z \sim 0.3 - 0.5$) redshifts, targeted toward restricted area
- NCP region, $5 - 100 \text{deg}^2$ area, 2-5 mK visibility noise level (1MHz x 30s sampling, ~ 1 month observation per declination)
- Mid-latitude (near CasA declination, to overlap with SDSS legacy spectroscopic survey, $1000 - 2000 \text{deg}^2$ area, $100 - 200 \text{deg}^2$ area overlap with SDSS)
- Detection of nearby $z \lesssim 0.05$ HI clumps : reliable estimates of number of detectable clumps (mass & redshift distribution)
- Detection of LSS in cross-correlation with optical survey
- Possible detection of LSS as excess auto-correlation signal ?

Some remarks

- Consider cross-correlation with ALFALFA or FAST HI survey, need survey at lower latitudes to have overlap with these surveys (Peter)
- There are frequency bands unusable due to strong RFI (from satellites), around 1380 MHz for example - We should blank these frequency bands which will decrease the statistical significance (Olivier)
- For section 3, evaluate the impact of going from analytical smooth beams to realistic beams from simulations - Peter hopes to have the computed beams soon
- Check whether the stripes observed by SDSS at the highest declinations (80deg) could be a target area (Albert)

2 LOW REDSHIFT SURVEYS

The Tianlai dish array reflectors are equipped with feeds having frequency bandwidth much larger than the instantaneous 100 MHz bandwidth of the digitisation and correlator system. The instrument observation band is defined by the

analog RF filters and this filter system can easily be modified to change the instrument frequency band. It is planned to tune the Tianlai Dish Pathfinder Array (T16DPA) frequency band to observe at low redshift, [1320, 1420] MHz or [1300, 1400] MHz, corresponding to the redshift range $0. \lesssim z \lesssim 0.076$ or $0.014 \lesssim z \lesssim 0.092$.

In addition, T16DPA dishes are fully steerable and equipped with an electronic pointing system. This allows targeted observations, although in transit mode, using T16DPA, in order to increase the integration time, thus the sensitivity, toward specific sky area. The North Celestial Pole (NCP), accessible to the Tianlai Dish Array represent several advantages and is an optimal target to carry deep, high sensitivity observations, as already suggested in (Zhang et al. 2016). A preliminary analysis of long duration observations of the NCP at $z \sim 1$ with T16DPA has also been presented in (Wu et al. 2021).

Low redshift surveys can be considered as a path to prove the effectiveness of the dense interferometric dish array and transit mode observations using the current Tianlai pathfinder instrument. For an Intensity Mapping survey to succeed, several instrumental and analysis challenges should be overcome, in particular:

- Precise determination of the instrument bandpass response
- Complex gain (amplitude and phase) calibration
- Electronic and environmental induced noise behaviour and its whitening
- Cross-coupling between feeds and correlated noise
- Array configuration, pointing errors
- Individual dish beam response shape knowledge and impact on visibilities and reconstructed 3D maps
- Overall instrument and calibration stability

As we shall discuss it in detail below, there are low- z extragalactic H_I signals, with structuring along the frequency similar to the cosmological LSS signals expected to be seen at higher redshifts, that will be within T16DPA sensitivity reach. The observation of these extragalactic signals would enable Tianlai to assess quantitatively the impact of the above instrumental effects on the recovered signal. We shall also show that it would be possible to determine the residuals from foreground subtraction and impact of individual antenna beam, and bandpass response on these residuals.

The advantage of observing at lower redshifts for T16DPA can be understood in two ways. On one hand, obviously, signals originating from extragalactic sources are much stronger at lower redshifts $z \sim 0.1 - 0.2$ than at redshifts $z \sim 1$, due to the signal strength decrease as $\propto d_L^{-2}(z)$ where $d_L(z)$ is the redshift dependent luminosity distance. However, one might argue that Intensity mapping do not observe individual sources, but aggregate emissions from neutral hydrogen in $100 - 1000 \text{ Mpc}^3$ voxels. Indeed, for a given setup, instrument angular resolution varies with redshift as $\propto (1+z)$, leading to transverse voxel size evolving as $\propto (1+z)^2 d_M(z)^2$, where d_M stands for the transverse comoving distance with $d_L = (1+z)d_M$ and $d_A = d_M/(1+z)$ (see e.g (Hogg 1999)). So ignoring cosmological evolution of sources, the average per voxel intensity would not vary with redshift. Nevertheless, considering the T16DPA angular resolution of $0.25^\circ - 0.5^\circ$, the voxel transverse size would range from $\sim 2 \text{ Mpc}$ at $z \sim 0.1$ to $\sim 10 \text{ Mpc}$ at $z \sim 0.5$. The voxel size thus exceeds even the cluster size at redshift 0.5, making

direct detection of individual structures (galaxies, clusters) by T16PDA, quite unlikely beyond $z \gtrsim 0.1$, as it would be shown in section 4.

What about statistical detection of LSS through the 3D map auto-correlation power spectrum? The LSS power spectrum changes slowly with redshift, contrary to distances. One might then expect that an IM instrument's ability to measure the LSS power spectrum would not change significantly with redshift. Unfortunately, the sensitivity to observe the cosmological LSS power spectrum decreases very quickly as redshift increases, due to the way the radio interferometer noise projects on sky. Indeed, a radio instrument, single dish or interferometer noise power spectrum, projected on sky as $P_{\text{noise}}(k)$ scales as (see for example (Ansari et al. 2012), section 3.2):

$$P_{\text{noise}}(k, z) \propto d_A^2(z) \frac{c}{H(z)} (1+z)^4 \quad (1)$$

$$\propto d_M^2(z) \frac{c}{H(z)} (1+z)^2 \quad (2)$$

This trend is defined by the mapping from instrument coordinates, the two angles defining a direction on sky and the frequency to a 3D position in a cosmological volume. We justify below in a slightly different way the noise power dependence with redshift. Let's consider brightness temperature sky maps $T_b(\alpha, \delta)$ with angular resolution $\delta\theta$ and frequency resolution $\delta\nu$. Instrument angular resolution $\delta\theta$ varies with wavelength $\delta\theta \propto \frac{\lambda}{D_{\text{array}}}$ where D_{array} is the array spatial extent and $\lambda = c/\nu$ the observation wavelength. Projecting such a map on a cosmological volume at redshift z , determined by the observation frequency ν , we obtain voxels with transverse a_\perp and radial a_\parallel comoving sizes, corresponding to a comoving volume $\delta V = a_\perp^2 \times a_\parallel$:

$$\frac{\nu_{21}}{\nu} = (1+z) \quad \nu_{21} = 1420.4 \text{ MHz} \quad (3)$$

$$\delta\theta = (1+z)\delta\theta_0 \quad \delta\theta_0 = \delta\theta(\nu = \nu_{21}) \quad (4)$$

$$a_\parallel = (1+z) \frac{c}{H(z)} \frac{\delta\nu}{\nu} = (1+z)^2 \frac{c}{H(z)} \frac{\delta\nu}{\nu_{21}} \quad (5)$$

$$a_\perp = (1+z)d_A(z)\delta\theta = d_M(z)\delta\theta \quad (6)$$

$$\delta V(z) = d_M^2(z) \frac{c}{H(z)} \frac{\delta\nu}{\nu_{21}} (1+z)^2 4(\delta\theta_0)^2 \quad (7)$$

Map pixel fluctuations due to instrumental noise, denoted σ_T^2 and characterised by the system temperature T_{sys} can be easily related to the noise power P_{noise} . Cosmological volume cell size (a_\perp, a_\parallel) determines the maximum accessible wave numbers (k_\perp, k_\parallel). Assuming white noise and ignoring damping due to per cell averaging, we can write the Plancherel-Parseval identity:

$$\sigma_T^2 = \sum_{k_x, k_y, k_z} |F(k_x, k_y, k_z)|^2$$

$$\sigma_T^2 \simeq P_{\text{noise}} \iiint^{k^{\text{max}}} dk_x dk_y dk_z$$

$$k_{\perp, \parallel}^{\text{max}} = \frac{2\pi}{2a_{\perp, \parallel}}$$

$$\sigma_T^2 \simeq P_{\text{noise}} k_x^{\text{max}} k_y^{\text{max}} k_z^{\text{max}}$$

$$\sigma_T^2 \simeq P_{\text{noise}} \left(\frac{2\pi}{2}\right)^3 \frac{1}{a_\perp^2 a_\parallel}$$

Check - some factor 2 might be missing, as the integral on k

should go over positive and negative frequencies We obtain then then the redshift dependence of cosmologically projected instrumental noise, which increases drastically with redshift:

$$P_{\text{noise}}(z) \simeq \frac{1}{\pi^3} \sigma_T^2 (a_{\perp}^2 a_{\parallel}) \quad (8)$$

$$P_{\text{noise}}(z) \simeq \frac{1}{\pi^3} (1+z)^2 d_M^2(z) \frac{c}{H(z)} \frac{\delta\nu}{\nu_{21}} (\delta\theta_0)^2 \times \sigma_T^2 \quad (9)$$

An survey of NCP by T16DPA would be sensitive to spherical harmonics $Y_{\ell,m}$ order ℓ in the range $75 \lesssim \ell \lesssim 850$ at $\nu \sim 1400$ MHz (see section 3), corresponding to angular scales $2\pi/\ell$. Taking into account evolution of the instrument angular scale range with redshift ($\ell \propto 1/(1+z)$), we obtain the survey transverse wave number sensitivity range:

$$k_{\perp}(z) = \frac{\ell(z)}{d_M(z)} \quad (10)$$

$$\ell^{\min}(z=0) \simeq 75 \quad \ell^{\max}(z=0) \simeq 850 \quad (11)$$

$$k_{\perp}^{\min,\max} = \frac{1}{(1+z) d_M(z)} \times \ell^{\min,\max}(z=0) \quad (12)$$

We have gathered in the table 1 the cosmological volume cell size, and the accessible transverse k_{\perp} range for an survey with angular scale sensitivities similar to T16DPA, map pixels with angular size 0.2° at $\nu \sim 1400$ MHz and frequency resolution 1MHz. The projected noise level as a function of redshift is shown in figure 2 as well as the accessible transverse k_{\perp} range for a T16DPA survey. The maximum value of the radial wave number k_{\parallel}^{\max} is also listed assuming voxels with $\delta\nu = 1$ MHz resolution. However, Tianlai dish array correlator computes visibilities with $\simeq 244$ kHz frequency resolution, so the survey could reach a maximum k_{\parallel} four times higher than the values listed in the table. Unfortunately, all the foreground subtraction methods rely of the smoothness of synchrotron emission with frequency and thus remove the signal modes with low k_{\parallel} . The simulations we have carried out here suggest a low cut-off value $k_{\parallel}^{\min} \sim 0.15 k_{\parallel}^{\max}$ (see section 3.3).

Figure 1 shows the radio sky near the NCP (North Celestial Pole), as it appears at 1350 MHz through the combination of Haslam synchrotron map (Haslam et al. 1981) and the sources from the NVSS catalog (Condon et al. 1998). The source closest to NCP, correspond to NVSS 011732+892848 with J2000 coordinates ($\alpha = 01h17m32.82s$, $\delta = +89d28m48.7s$) with a flux ~ 2 Jy at 1.4 GHz. It is likely associated to the 6C B004713+891245 source identified in the Sixth Cambridge catalog (Baldwin et al. 1985) with a flux of $\sim 7-8$ Jy at 152 MHz. The brightest source visible in the map is the 3C 061.1 FR-II radio-galaxy with J2000 coordinates ($\alpha = 02h22m35.046s$, $\delta = +86d19m06.17s$), and redshift $z = 0.18781^1$ resolved into three sources in NVSS, with a total flux exceeding 6 Jy at 1.4 GHz, and 8-10 Jy at 750 MHz.

The visibility simulation and 3D map reconstruction is briefly described in the next section, as well as the simple foreground subtraction methods we have used. We will then show that it is possible to detect individual galaxies or group of galaxies at very low redshifts $z \lesssim 0.05$ in the NCP region. We have also studied the statistical detection of the LSS through cross-correlation with optical surveys, as discussed

z	d_M	a_{\perp}	a_{\parallel}	k_{\perp}^{\min}	k_{\perp}^{\max}	k_{\parallel}^{\max}	P_{noise}
0.1	451	1.7	3.7	0.16	1.9	0.85	4
0.2	880	3.7	4.2	0.08	0.96	0.75	20
0.5	2028	10.6	5.5	0.037	0.42	0.57	200
1.0	3536	24.7	7.3	0.021	0.24	0.43	1430
2.0	5521	57.8	9.7	0.013	0.15	0.32	10400

Table 1. The comoving radial distances, cosmological transverse and radial cell size corresponding to angular cell size $0.2^\circ \times 0.2^\circ \times 1$ MHz at $z = 0$. Distances in units of Mpc/h₇₀ and k in h₇₀Mpc⁻¹ and P_{noise} in mK²/(Mpc/h₇₀)³, assuming a per pixel noise of $\sigma_T^2 \sim 10$ mK². The values listed for k_{\parallel}^{\max} assume 1MHz frequency resolution. The foreground subtraction introduces a low cut-off for k_{\parallel} - see text.

in section 5. A mid latitude survey, covering a larger area would be less sensitive due to higher noise level, but even more so due to much larger residuals from imperfect foreground subtraction, as discussed in the next section. However, thanks to the larger area, it is also possible to detect the cross-correlation signal.

- Explore also some aspects of component separation (foreground subtraction)
- Discuss the way instrument noise (radiometer equation) project on sky - when observations are discussed as cosmological power spectrum $P(k)$: variations with redshift - Discuss also the accessible k-range (wave-number) - depending on the survey area and instrument configuration ($k_{\perp} k_{\parallel}$).
- Present the the three cosmological signals we might aim for : direct detection of HI clumps at very low redshifts ($z < 0.05$), cross-correlation with optical surveys and possible LSS detection in auto-correlation at $z \sim 0.4$.

¹ NED query for object name 3C 061.1 - <https://ned.ipac.caltech.edu/>

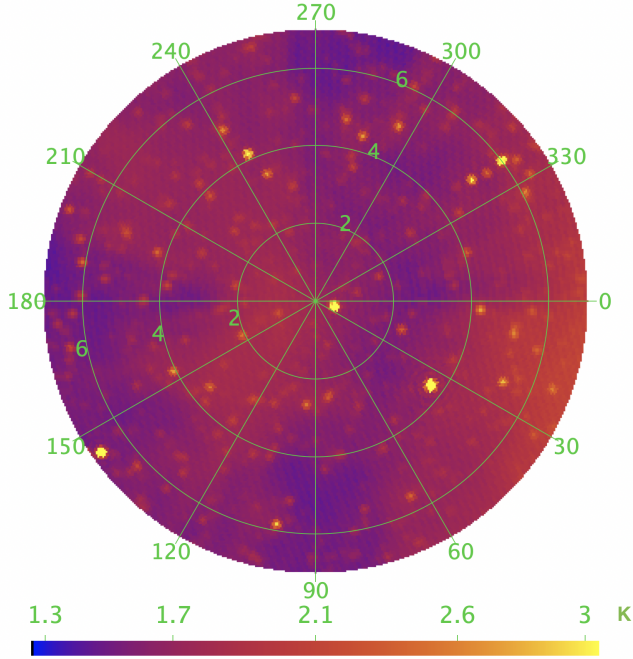


Figure 1. Foreground map of a 7 deg. radius region around NCP at 1350 MHz, smoothed with a 15arcmin resolution gaussian beam. Haslam map of diffuse emission at 408 MHz as well as NVSS radio sources, extrapolated to 1350 MHz with a spectral index $\beta = -2$. Color scale corresponds to temperature in Kelvin.

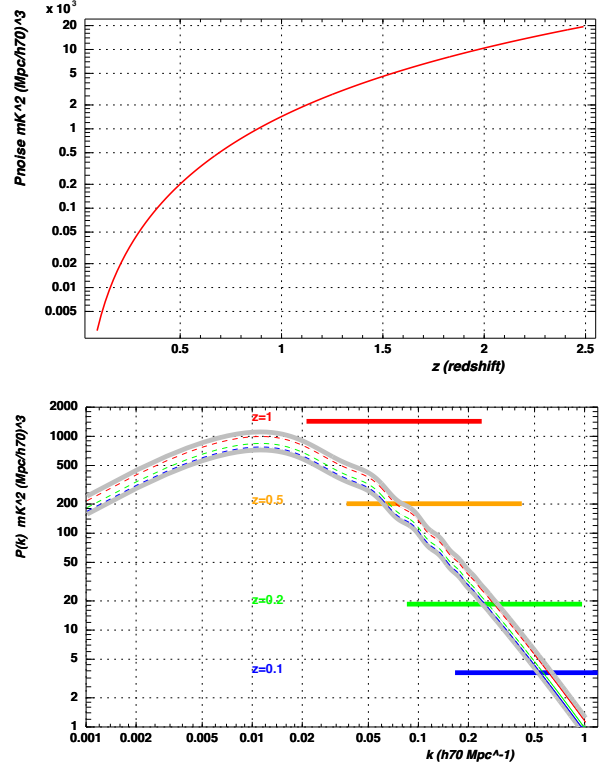


Figure 2. Top: White noise power spectrum $P_{\text{noise}}(z)$ level as a function of redshift for a survey similar to T16DPA with an angular map pixel size of 0.2° and 1MHz, and for per pixel noise level $\sigma_T^2 = 10\text{mK}^2$. Bottom: Projected noise power spectrum $P_{\text{noise}}(k)$ and the accessible transverse k_\perp range for a survey of the NCP region by T16DPA.

3 SURVEY SENSITIVITY

3.1 Simulation and analysis pipeline

The JSkyMap² package has been used for computing visibilities for the Tianlai dish array setup and the survey strategies studied in this paper. The package provides also several tools for reconstructing maps from transit visibilities. Here, we have used the m-mode visibility computation and map making tools, which operates in the spherical harmonics space $Y_{\ell,m}$ as described in (Zhang et al. 2016) and (Shaw et al. 2015). The simulation and analysis pipeline includes several other C++ or python software modules, which handles the preparation of the input data, such as the generation of H_I sources from optical catalogs, foreground subtraction, source detection, power spectrum computation and optical - radio cross-correlation computation.

The study presented here uses only intensity maps, ignoring polarisation. Foreground has been modeled through a combination of the diffuse synchrotron emission, represented by the reprocessed Haslam map at 408 MHz (Remazeilles et al. 2015) and the radio sources from the NVSS catalog

² JSkyMap: <https://gitlab.in2p3.fr/SCosmoTools/JSkyMap> (check the wiki pages)

(Condon et al. 1998). In practice, for each simulated observation frequency, diffuse synchrotron emission and radio-sources have been extrapolated from their reference frequencies, (408 MHz and 1400 MHz) using a fixed value of the spectral index $\beta \sim -2 \dots -2.5$. All sources with flux larger than 0.05Jy and $\delta > 15^\circ$ have been included in the simulation.

The array configuration corresponds to the actual positions of the antennae in the array, and we have used a frequency dependent Bessel J_1 single dish response, with azimuthal symmetry and an effective dish diameter $D_{\text{eff}} = 5.6m$. The beam response used here is represented for $f = 1350$ MHz in the figure 3. There are 120 different baselines, excluding auto-correlations and ignoring polarisation. Visibilities have been computed with a time sampling $\delta t = 30$ s and we have generally considered a $\delta\nu = 1$ MHz frequency resolution. Two surveys have been studied here, spanning a total duration of several months, up to two years.

(i) A survey of the NCP region with 4 constant declination scans $\delta = 90^\circ, 88^\circ, 86^\circ, 84^\circ$, and covering an area of about 100 deg^2 around the north pole. We have generally used a fiducial area within 7 deg. from the north pole, $\delta > 83^\circ$, which would yield a surveyed area $\sim 150 \text{ deg}^2$. The simulated visibility data set for each simulated frequency plane and for each case represents thus a total number of time samples: $\sim 4(\delta) \times 120(\text{visi}) \times 2800(\text{time}) \simeq 1.35 \cdot 10^6$

(ii) A Survey in mid-latitude area, covering a much larger portion of sky, using 6 constant declination scans at $\delta = 49^\circ, 51^\circ, 53^\circ, 55^\circ, 57^\circ, 59^\circ$, covering a 12° band in declination $48^\circ \leq \delta \leq 60^\circ$, representing about $\sim 12\%$ of the sky or $\sim 2500 \text{ deg}^2$. However, we have excluded a region in right ascension contaminated by the galactic plane and bright sources such as CasA and CygA when computing noise power spectrum and mode mixing residuals. The fiducial area used $40^\circ < \alpha < 260^\circ$ represents about 1500 deg^2 . The visibility data set represents about $2 \cdot 10^6$ time samples per frequency plane and for each simulated case.

The T16DPA noise system temperature has been determined to be $T_{\text{sys}} \sim 80$ K Wu et al. (2021). The simulations here have been carried out with a fiducial noise level of 5 mK per $\delta t = 30$ s visibility samples, and for a $\delta\nu = 1$ MHz frequency band. Such a noise level should indeed be reached after ~ 10 days (more precisely 8.5×24 hours spent on each constant declination scan, corresponding to a total integration time $t_{\text{int}} = 8.5 \times 30 \simeq (256 = 16^2)$ s per visibility samples, leading to a noise level :

$$\sigma_{V_{ij}} = \frac{T_{\text{sys}}}{\sqrt{t_{\text{int}} \delta\nu}} = \frac{80 \text{ mK}}{16} = 5 \text{ mK}$$

Tianlai day time data is contaminated by the sun signal leaking through far side lobes, it is therefore planned to use only night time data. T16DPA should thus be able to reach this 5mK by surveying the NCP region during two periods of 1.5 month each, separated by 6 months. 10 days would be spent on each of the four declinations, corresponding to a total of 40 days, or about 1.5 month, and the operation would be repeated six months later, to get full night time coverage of the 24 hours RA range. A noise level of 2.5mK would also be reachable by observing the NCP area over a full year, to get 2×40 days per declination observation time, so a total of $2 \times 4 \times 40 = 320$ days.

For each frequency plane, a spherical map is recon-

structed through m-mode map making, or rather, the linear system of equations relating visibilities to the input sky is solved in spherical harmonics $a_{\ell,m}$ space. A pseudo-inverse method is used in JSkyMap package and the numerical stability of the inversion process, as well as the noise level are controlled through parameters which define the ratio r_{PSI} of smallest to largest eigenvalue for each inversion, as well as an absolute threshold on the minimal eigenvalue λ_{PSI} . The two values has been set to $r_{\text{PSI}} = 0.02$ and $\lambda_{\text{PSI}} = 0.001$ for the analysis presented here, which can be considered as a medium level.

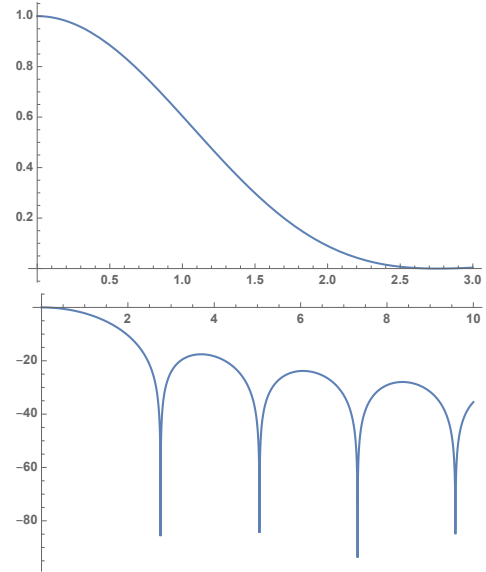


Figure 3. Beam response (Bessel J_1) as a function of the polar axis θ in degrees, with respect to the beam axis (antenna pointing direction) at $f = 1350$ MHz. top: main beam, in linear scale; bottom: main beam and side lobes, in logarithmic scale (dB).

We have used spherical maps with a resolution of 5 arcmin for the reconstructed maps, although the array angular resolution is closer to 10 – 15 arcmin, as stated in section 2. The reconstructed map pixels have thus a certain level of redundancy, with pixel to pixel noise values being correlated for neighboring pixels, but these higher resolution maps showed a slight advantage for source detection and foreground removal. We have used a the **SphereThetaPhi** pixelisation scheme, which features almost square and equal area pixels along θ, ϕ directions, instead of the more standard HEALPix scheme. This pixelisation scheme, available in the SOPHYA³ library, sometimes called IGLOO pixelisation, preserves to some extent the symmetry around a pixel located exactly at the pole $\theta = 0$ and has also the advantage of being fully flexible in terms of angular resolution or the pixel size.

We perform also an optional filtering step in the spherical harmonics space $a_{\ell,m}$, before map reconstruction and foreground subtraction. The quality of the reconstruction degrades at the two ends of the T16DPA ℓ sensitivity range.

³ SOPHYA c++ class library <http://www.sophya.org>

At low ℓ , this is explained by the absence of the autocorrelation signal which is not used in map reconstruction, and the minimal baseline length, about 8.8m limits the sensitivity below $\ell \lesssim 75$ for the NCP survey. At the other end, map reconstruction quality and hence the noise level increases for angular resolution corresponding to the array size, for $\ell \gtrsim 850$ for the NCP survey. We have smoothly damped $a_{\ell m}$ coefficients for $\ell \lesssim 75$ and $\ell \gtrsim 875$. A gaussian filter with $\sigma_\ell = 750$ has also been applied, and all $m = 0$ modes have been put to zero. This last filter is intended to remove wiggles with near perfect azimuthal symmetry which appears due to the partial sky coverage combined with limited sensitivity range in ℓ .

Figure 4 shows an example of reconstructed map, after (ℓ, m) space filtering at a frequency of $f = 1350\text{MHz}$. Sources present in the *true* sky map (figure 1), as well as larger structures, are clearly visible, while the noise level ($2 - 4\text{ mK}$) is too low to be noticeable. Some artefacts, such as rings around bright sources can easily be seen and are due to incomplete (ℓ, m) plane coverage and filtering. A patch of sky, as reconstructed from Tianlai dish array survey of a mid-latitude area is shown in the top panel of figure 5. Despite significantly higher noise level ($\sim 15\text{ mK}$), it is not noticeable on this reconstructed map, where brightest sources are a few Jy.

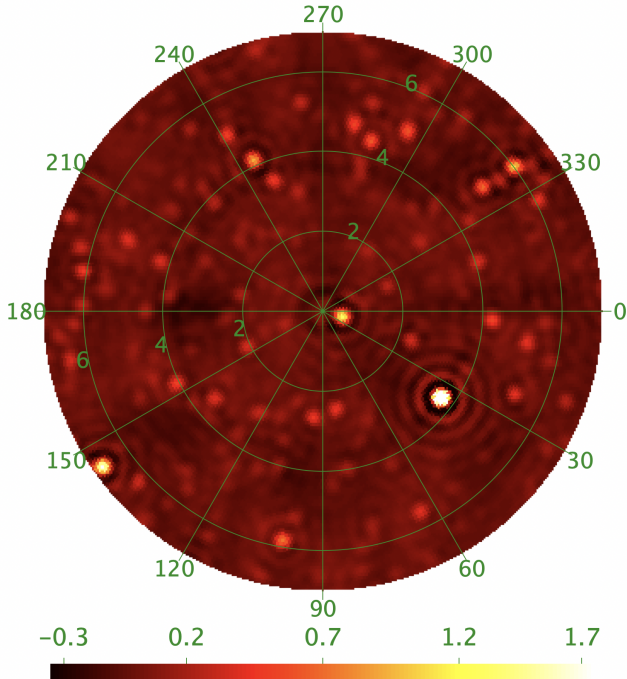


Figure 4. Reconstructed map of the NCP region, as observed by T16DPA at $f = 1350\text{MHz}$. This is a the 7 deg. radius around $\delta = 90^\circ$, extracted from the reconstructed spherical map using m-mode map making and after (ℓ, m) space filtering.

Average reconstructed sky angular power spectrum of the NCP region is shown in figure 6. The sky power spectrum is higher at larger angular scales, with an overall level about $\sim 1\text{K}$. Effect of the instrument and map making ℓ -space re-

sponse is visible at the two ends, $\ell \lesssim 50$ and $\ell \gtrsim 1150$ (grey curve). The additional effect of (ℓ, m) can clearly be seen comparing the sky power spectrum after filtering (in black) and before filtering (grey curve). The projected noise angular power spectrum $C_{\text{noise}}(\ell)$ is also shown on this figure. These $C_{\text{noise}}(\ell)$ have been computed from maps reconstructed from white noise-only visibilities, with a RMS fluctuation level of 5mK per $\delta\alpha = 30\text{s}$ visibility samples. As expected, the noise spectrum increases significantly toward the high- ℓ end of the spectral sensitivity range, above $\ell \gtrsim 800$. This is due first to the decrease of the redundancy of baselines, and then, an incomplete coverage of wave modes or (ℓ, m) plane at the high- ℓ end. The effect of (ℓ, m) filtering on the noise power spectrum $C_{\text{noise}}(\ell)$ can be seen comparing the orange curve, before filtering, with the red curve, after filtering.

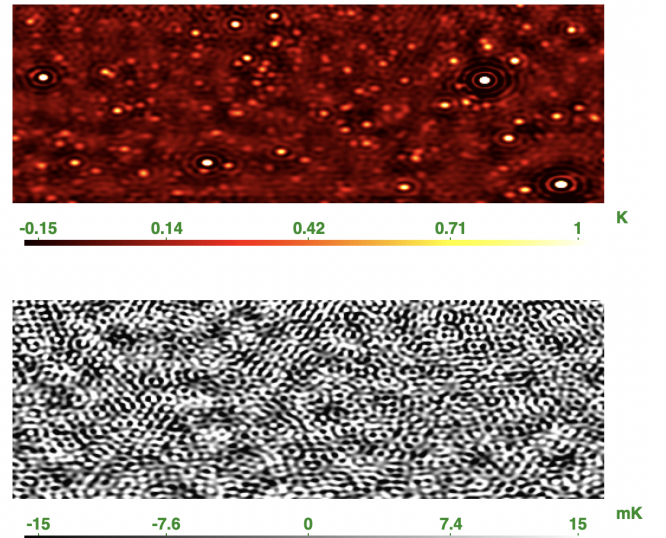


Figure 5. Reconstructed map (top) and noise map (bottom) of the mid-latitude region, after (ℓ, m) filtering, as observed by T16DPA at $f = 1350\text{MHz}$. The patch of sky shown covers the declination range $43^\circ < \delta < 57^\circ$ and the right ascension range $90^\circ < \alpha < 130^\circ$, with 5 arcmin pixel size.

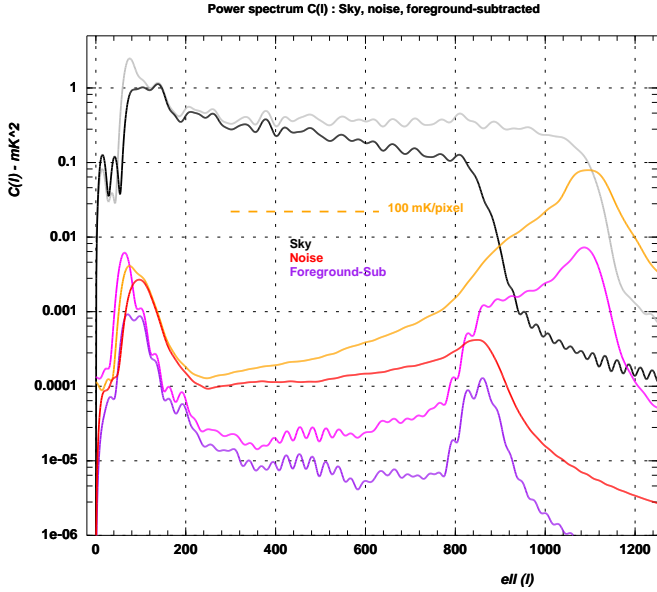


Figure 6. Average angular power spectrum $C(\ell)$ from the a data cube of 100 reconstructed maps of the NCP region, covering an area with 7 deg. radius around NCP, and the frequency range 1300-1400 MHz. The reconstructed sky power spectrum is shown in black, noise power spectrum in red and residual power spectrum after foreground subtraction in purple, after filtering in (ℓ, m) plane. Curves in lighter colors (grey, orange and light purple) show the power spectrum from maps without (ℓ, m) plane filter.

3.2 Foreground subtraction

Our aim here is not to devise the best foreground subtraction method, but rather characterise the instrument and survey strategy sensitivity and the corresponding performance for mitigating the mode mixing. Two simple foreground subtraction methods have been used here which exploits the synchrotron dominated foreground smoothness with frequency. The first method (**P**) represents the synchrotron emission frequency dependence as a second degree polynomial in frequency. The coefficients are determined for each direction through a linear χ^2 fit to the measured temperatures, and the resulting fitted foreground $T_{\alpha,\delta}^{\text{fgnd-P}}(\nu)$ is then from the 3D temperature map:

$$T_{\alpha,\delta}^{\text{fgnd-P}}(\nu) = A_{(\alpha,\delta)}\nu^2 + B_{(\alpha,\delta)}\nu + C_{(\alpha,\delta)} \quad (13)$$

$$T^{\text{P}}(\alpha, \delta, \nu) = T(\alpha, \delta, \nu) - T_{\alpha,\delta}^{\text{fgnd-P}}(\nu) \quad (14)$$

The second method (**DF**) is a very simple difference filter along the frequency. For each frequency plane, we subtract the average of two nearby frequency planes at ν_-, ν_+ , with a specified frequency gap $\Delta\nu$, $\nu_- = \nu - \Delta\nu$ and $\nu_+ = \nu + \Delta\nu$. We have used $\Delta\nu = 2\text{MHz}$ throughout this paper.

$$T_{\alpha,\delta}^{\text{fgnd-DF}}(\nu) = \frac{1}{2}(T(\alpha, \delta, \nu_-) + T(\alpha, \delta, \nu_+)) \quad (15)$$

$$T^{\text{DF}}(\alpha, \delta, \nu) = T(\alpha, \delta, \nu) - T_{\alpha,\delta}^{\text{fgnd-DF}}(\nu) \quad (16)$$

We have represented the average angular power spectrum of the residual signal $C_{\text{res}}(\ell)$, after foreground subtraction for the two methods (P,DF), for the NCP survey on the

left panel of figure 8. A set of 100 sky maps, reconstructed from mock visibilities, corresponding to four constant declination scans at or near the NCP, and after (ℓ, m) plane filtering have been used. Compared to the input sky angular power spectrum $C_{\text{sky}}(\ell)$ shown as the black curve, one can see that the foreground angular power spectrum is suppressed by a factor $\gtrsim 20000$ for the polynomial subtracted foreground (P), and $\gtrsim 60000$ for the difference along frequency filter (DF method). These values correspond to a factor ~ 150 (P) and ~ 250 (DF) damping in amplitude for temperature fluctuations due to foreground. While this might not be sufficient for the direct detection of the cosmological 21cm signal, the foreground residuals due to mode mixing and imperfect subtraction would be well below the instrumental noise level for the NCP survey by Tianlai.

However, T16DPA becomes less efficient to fight mode mixing for a mid-latitude survey. We have shown the angular power spectrum of the residual after foreground subtraction using the DF method, for a mid-latitude survey, on figure 9. A set of three reconstructed maps at $f_{-2} = 1348\text{MHz}$, $f_0 = 1350\text{MHz}$ and $f_{+2} = 1352\text{MHz}$ have been used for the power spectra shown on this figure. The fiducial area used to compute the power spectra excludes right ascension ranges corresponding to the Galactic plane or contaminated by CasA and CygA and represents about 1500deg^2 . Comparing the black curve, which represents the reconstructed $C_{\text{sky}}(\ell)$ of the diffuse synchrotron and radio sources and violet curve $C_{\text{res}}(\ell)$, corresponding to the residuals after foreground subtraction through the DF method, we see that the $C(\ell)$ power spectrum has been damped by a factor ~ 1200 , or about ~ 35 for the temperature fluctuation amplitude. The residual after foreground subtraction reaches a level similar to the noise on the map, with RMS fluctuations $\sim 15\text{mK}$.

This damping factor, about 50 times lower, or 7 times lower in amplitude, is explained by a higher level of mode-mixing for a mid-latitude survey by Tianlai, compared to the NCP case. Indeed, one can consider that for observations toward NCP, the projected baselines changes with the sky rotation, improving map making performance in terms of individual mode reconstruction. The circular configuration of T16DPA was optimised for a good coverage of the angular sky modes or the (u, v) , minimising the redundant baselines, compared to a regular rectangular grid configuration for example. Although arrays with redundant baselines offer advantages for the gain and phase calibration, they should exhibit higher level of mode mixing. For very large arrays, with several hundred or several thousand elements, a combination of redundant and non redundant baselines should be used to mitigate both mode mixing and calibration issues.

3.3 Noise level and survey sensitivity

The left panel of figure 7 shows an example of noise map for the Tianlai NCP survey, while the histogram of the corresponding pixel value distribution is shown on the right panel. The pixel to pixel temperature fluctuation is about 4mK , and even about 2.2mK for the central 3° radius area, and for a 5mK noise level per 30s visibility samples. The bottom panel of figure 5 shows a similar noise map for the mid-latitude survey, with an RMS pixel fluctuation level of $\sim 16\text{mK}$. The noise level scales slightly faster than the square root of the

ratio of the surveyed sky area, $(2500\text{deg}^2/150\text{deg}^2 \simeq 16)$, as the mid latitude survey discussed here requires 6 constant declination scans, hence 50% more observing time.

As mentioned already, the maps with 5arcmin pixels used here have higher resolution than the effective instrument and reconstruction angular resolution, limited to about $\ell^{\text{max}} \sim 850$ or 12arcmin. The noise correlation between neighbouring pixels is visible on the noise maps, and compatible with the noise angular power spectrum $C_{\text{noise}}(\ell)$. For the NCP survey, the noise power spectrum is nearly flat for $200 < \ell < 800$, and 15-40 higher than the foreground subtraction residuals, as shown in the left panel of figure 8. Tianlai should be able to get noise dominated foreground subtracted maps for the NCP region, even for a deep NCP survey, reaching $\sim 2\text{mK}$ per pixel noise level, for a survey where each of the 4 declinations would be observed during $2 \times 40 \times 24\text{hours}$.

The right panel of figure 8 shows the sky and residual after foreground subtraction radial mode power spectra $P(\tau)$ for the NCP survey. These have been obtained computing the average spectrum obtained through a Fourier Transform (FFT) along the frequency direction, for each direction of sky. The Fourier wave modes along the frequency correspond to a time and are sometimes referred to as the delay τ . Given the 100 MHz bandwidth, with 100 frequency planes, the frequency waves modes, or delay, cover the range from $\tau_1 = 10\text{ns}$ to $\tau_{50} = 500\text{ns}$. The black curve represents the average reconstructed sky $P_{\text{sky}}(\tau)$, with the power highly concentrated at very low delay modes ($\tau \lesssim 20 - 30\text{ns}$), but with still significant power up to $\tau \lesssim 100\text{ns}$. The effect of the two foreground subtraction methods, and their τ -response can be understood by looking at the shape of the average delay-spectrum of the residual maps without noise (purple curves), or the ones with noise (orange/red). The latter are noise dominated and it can be seen that the polynomial foreground subtraction (P) removes delay-modes below $\tau \lesssim 50 - 60\text{ns}$, while the differential filter along frequency (DF) can be considered as a band pass filter, removing $\tau \lesssim 100\text{ns}$ and $\tau \gtrsim 400\text{ns}$. The (DF) method is more effective at removing foreground modes at low delay, but leads to noisier maps. In addition to removing low-delay modes, the polynomial subtraction method (P) damps the power $P(\tau)$ by a factor about 30 for all modes $\tau > 100\text{ns}$.

So far, we have assumed a perfect knowledge of the instrument response, specially the individual antenna angular response, instrument frequency and relative gain and phase calibration. Discussion of impact of an imperfect knowledge of the instrument response on the survey performance is beyond the scope of this paper. However, preliminary studies suggest that one should be able to cope with lack of knowledge of individual antenna side lobes for the NCP survey, if the main lobe is well modeled. On the other hand, phase calibration errors can significantly degrade the instrument ability to remove foregrounds. To illustrate this, we have included the green curves in figure 8 which show the average power spectrum of the foreground subtracted maps, in the presence of phase calibration errors. To obtain these curves, we have applied a relative phase error, drawn independently for each baseline and each frequency, according to a zero-mean normal distribution with an RMS of 7° . In this case, the residual maps would be dominated by foreground con-

tribution, with a power spectrum $C_{\text{res}}(\ell)$ 10 times larger than the one due to the instrument noise.

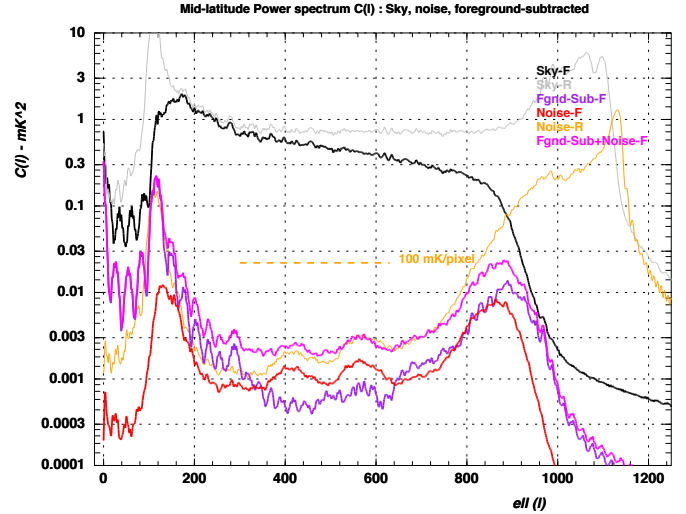


Figure 9. Sky, noise and residual after foreground subtraction angular power spectrum $C(\ell)$ for the mid-latitude survey. These power spectra have been computed from a set of three frequency maps at 1348, 1350, 1352 MHz and the differential filter along the frequency (DF) foreground subtraction method has been used for this plot.

left from the original paper plan - remove once done

- Describe the visibility simulation and map reconstruction process
- Describe and discuss the two foreground subtraction method used here
 - per pixel noise level (visibility space and map space)
 - Impact of imperfect calibration - (phase and amplitude calibration errors)
 - illustrate for the NCP case, as well as lower latitude case

4 H_I CLUMP DETECTION

mass distribution and effective detection thresholds (based on simulation including foregrounds and radio-sources, followed by map-making, or in visibility space)

The aim of this analysis is to assess the number of direct detection of H_I clumps in a low- z survey of either a mid-latitude band or a circular region around the North Celestial Pole with T16DPA. We first estimate the H_I clumps detection efficiency as a function of their apparent flux for the NCP and mid-latitude cases. In a second step we combine these detection thresholds in the flux domain with the H_I mass function to extract the number of H_I that could be detected, assuming a spatial uniform random distribution, for the NCP and mid-latitude cases.

4.1 H_I clumps flux detection thresholds

To assess the detection efficiency for point-like H_I sources we have used a pipeline sharing most of the ingredients de-

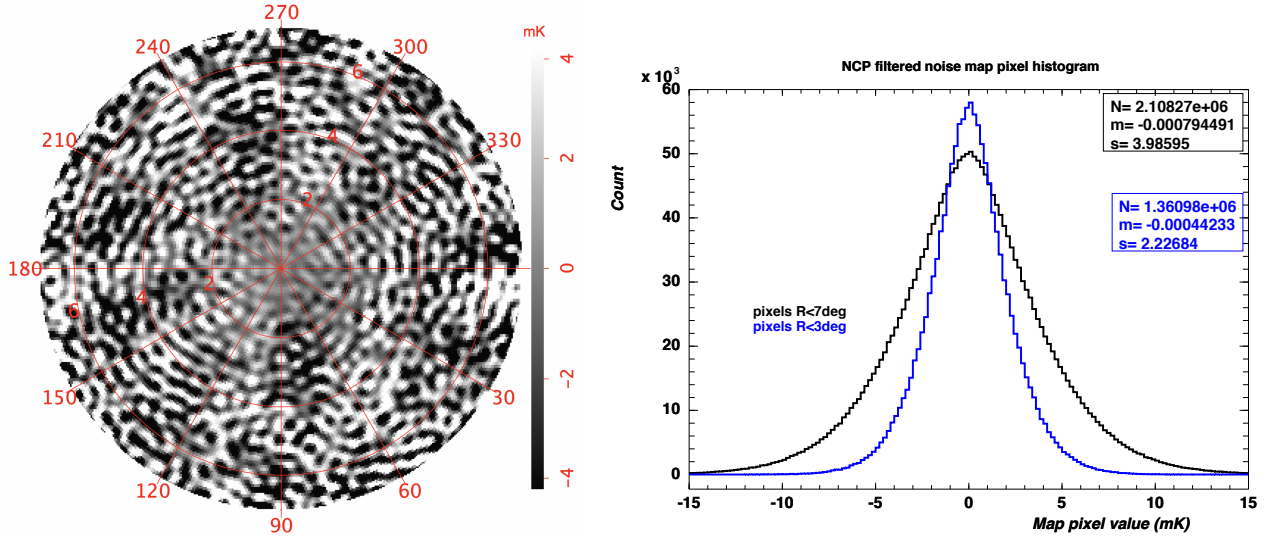


Figure 7. Left: Noise map after reconstruction with (ℓ, m) filtering of the NCP region covering an area with 7 deg. radius at $f = 1350\text{MHz}$ (map scale in mK). Right: Noise map pixel value distribution, in black for the full 7 deg. radius map around NCP, and blue, restricted to the central 3 deg. radius, covering $\sim 30\text{deg}^2$. Note that restricted area corresponding to the blue histogram correspond to $\sim 18\%$ of the full area; The blue histogram has been rescaled to enhance the figure readability

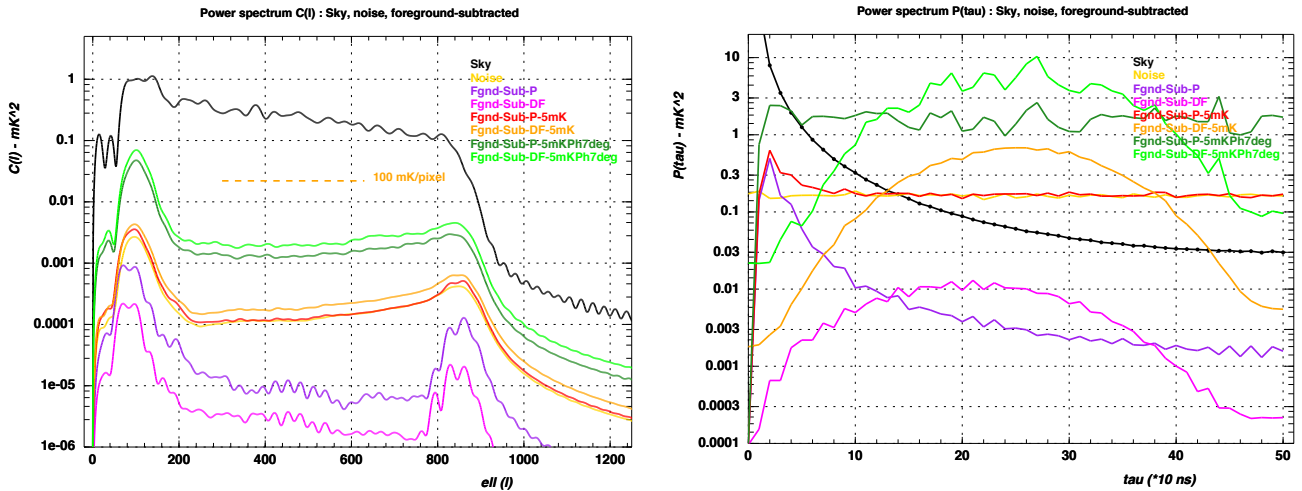


Figure 8. Left: average angular power spectrum $C(\ell)$ from the a data cube of 100 reconstructed maps, with (ℓ, m) filtering of the NCP region covering an area with 7 deg. radius around NCP, and the frequency range 1300-1400 MHz. Right: average power spectrum along the frequency axis $P(\tau)$. The reconstructed sky power spectrum is shown in black, noise power spectrum in gold and residual power spectrum after foreground subtraction in purple without noise, and in red with noise. The green curve shows the effect of phase calibration errors (7 degree RMS gaussian phase errors) on the residuals after foreground subtraction.

scribed in section 3.1. We simulate observations of the NCP and mid-latitude surveys as described there, for only three frequencies : 1348, 1350 and 1342 MHz.

To the generic astrophysical components (diffuse synchrotron Galactic emission , and continuum NVSS sources) we add, for the central frequency a set of uniformly distributed point-like sources of a given flux. For each frequency we compute simulated visibilities, project them into sky maps and then filter them, as explained in 3.1. The noise level per visibility sample (30s integration time) used in the following is 5mK. To roughly account for foreground subtraction, we subtract from the central frequency map the average of the two outer frequency ones. Finally, we repro-

ject the difference into rectangular (mid-latitude case) or square (NCP case) maps using simple projections. For the mid-latitude difference maps, we include in the pipeline a loose high-pass filter in spacial frequency domain to reduce some foreground subtraction and projection residuals.

The final step is the sources detection. We use a basic scheme based on the `DAOSTarFinder` class from the `photutils` Python package (Bradley et al. 2021). As the map foreground subtraction and map reconstruction and projection leave some artefacts in the residual maps, we set loose sphericity criteria to this detector. We set the detection threshold relatively to the map's RMS, at 7 (NCP) and 10 (mid-latitude)times this value to avoid spurious detections

Dataset	α	m_*	ϕ_*
Full	-1.25 ± 0.02	9.94 ± 0.01	$.0045 \pm .0002$
Near	-1.22 ± 0.02	9.76 ± 0.04	$.0062 \pm .0005$

Table 2. HI mass function parameters fitted using the whole ALFALFA dataset and its near subset

on reconstruction-induced high spacial frequency residuals. To assess the detection efficiency, we count the number of detected sources within 2 pixels (CHECK THIS) of the simulated ones. In the NCP case, we simulated 5 sources over the 7 (TBC) degrees circular observed region, but repeat this operation 20 times to reach an accuracy of a few percents. In the mid-latitude case, the rectangular surveyed area is much larger so that this repetition is not needed more than 2 or 3 times.

The detection efficiencies we measure in the NCP and mid-latitude simulations are reported on figure 4.1. Thanks to the higher integration time per map pixel in the NCP case, these results show that the detection threshold is much lower in the NCP case wrt the mid-latitude one : about .1 and 1.2 Jy, respectively. We have in each case fitted the detection efficiency vs flux variations with an error function ; these fits will be used in the computation of the expected number of HI clump direct detections in the low- z Tianlai survey.

4.2 Number of expected H_I clumps observations

We assume the H_I clumps population to be randomly spatially distributed and to follow the characteristics measured using ALFALFA survey data in Jones et al. (2018). As shown in this paper, the mass function (MF) of the HI clumps - the number density of galaxies falling in a logarithmic HI mass bin, is well described by a Schechter function :

$$\begin{aligned} \phi(M_{HI}) &= \ln(10)\phi^* \left(\frac{M_{HI}}{M_*}\right)^{\alpha+1} \exp\left(-\frac{M_{HI}}{M_*}\right) \\ &= \frac{dN_{ga}}{dV d\log_{10}(M_{HI})} \end{aligned} \quad (17)$$

The parameters in this equation are ϕ^* (normalisation), M_* ('knee' mass ; we use in the following the reduced parameter $m_* = \log(M_*/M_\odot)$) and α , defining the low-mass slope of this distribution. Jones et al. (2018) fit these parameters using several subsets of the ALFALFA clump dataset ; these results show some spatial dependence. We will retain here the parameters fitted with the whole dataset (ALFALFA 100%) and its 'near' subset ($v_{CMB} < 4000\text{km/s}$), listed in Table 2. The difference between the "full" and "near" parameter may give an indication of the systematics linked to the HI mass function. ALFALFA also observed some variation of these parameters in different regions on the sky but we do consider different areas in this study, therefore we stick to this global variation with observed distance in the following.

The relationship between the HI mass and flux is also reported in Jones et al. (2018) :

$$\frac{M_{HI}}{M_\odot} = 2.356 \cdot 10^5 D_{Mpc}^2 S_{21} \quad (18)$$

where D_{Mpc} is the distance to the source in Mpc and S_{21}

Dataset	NCP	mid-latitude
Surface (deg ²)	100	1500
HI clumps/deg ² (full MF)	.048	.0012
HI clumps/deg ² (near MF)	.035	.0009

Table 3. Number of expected HI clump discoveries per square degree for the NCP and mid-latitude surveys, for the two parametrizations of the HI mass function given in table 2. We also give an order of magnitude of the sky surface covered in each of these surveys.

the integrated 21cm flux in Jy.km/s. For each redshift value, we compute D using a fiducial cosmology (Planck 2015). Using this distance and assuming a $\sim 210\text{km/s}$ velocity width (corresponding to $\sim 1\text{MHz}$ in the frequency domain) we can translate the flux limits or detection efficiencies in Jy into HI mass limits or detection efficiencies at each redshift. The integral of the HI mass function convolved with such detection efficiency gives the number of expected detections at any given redshift ; the sum of these contributions finally gives the total number of expected detections.

We present the expected number of HI clump detections per squared degree for the NCP (left-) and mid-latitude case (right hand side) as a function of redshift, assuming the HI mass function parameters from ALFALFA (full sample) on figure 4.2. The total number of detections per square degrees are reported on this figure and also in table 3. As can be seen from the plots shown on figure 4.2 the expected redshifts of the HI clumps detected are very low : below .02 for the NCP case, and .005 in the mid-latitude case. This is at first order irrespective of the HI mass function parameters used. At these very low redshifts it may therefore be justified to use the 'near' HI mass function parameters from ALFALFA. As the knee mass is somewhat lower in that case, this results in lower number of expected detections, as reported in table 3.

In the mid-latitude case, the larger dilution of the observations on the sky results in a higher detection threshold, hence a lower expected redshift and number of detections than in the NCP case. This is not totally compensated by the much larger surface covered by this survey, making the NCP survey the most promising in terms of expected HI clump discovery rate. As mentioned in section 3 a lower noise per visibility sample may be achieved by observing over longer periods. This would increase the number of expected HI clumps, but only in the NCP case where the noise dominates the reconstruction artefacts in the reconstructed maps.

5 CROSS-CORRELATION WITH OPTICAL GALAXY CATALOGS

discuss LSS in cross correlation with optical surveys , at mid-latitude, with SDSS , NCSS for NCP :

- discuss the possible scenarios : NCP, mid latitude , cross correlation with SDSS ,
- show optical catalog redshift distribution.
- effect of incomplete spectroscopic catalogs
- effect of redshift errors

In this section we explore the prospects for extracting the cross-correlation signal between the Tianlai low redshift

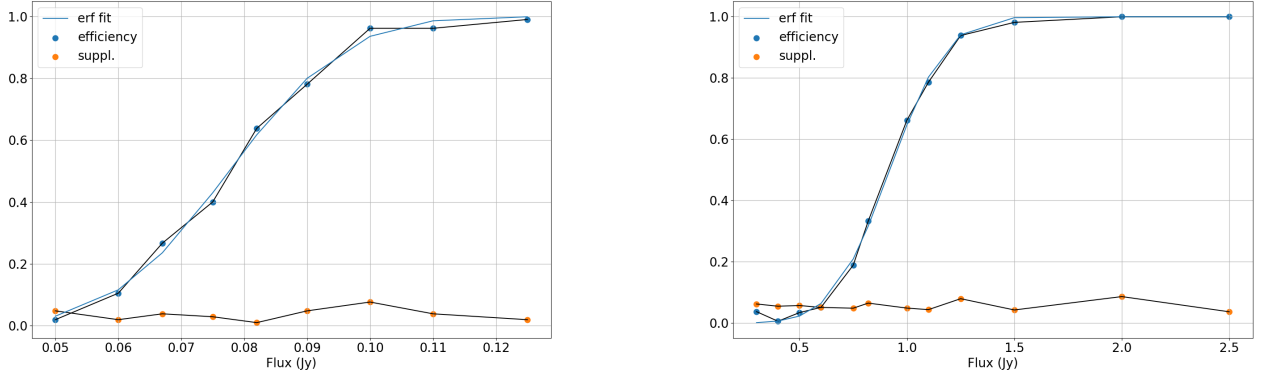


Figure 10. HI clump detection efficiencies as a function of flux, for the NCP (left-) and mid-latitude (right hand side) measured by our simulations. On each part we represent as blue dots the efficiencies measured at each simulated flux. the read dots correspond to the number of spurious detection (detections located farther than 2 pixels from the simulated clumps positions). The cyan curve is a fit of the efficiencies values with an error function.

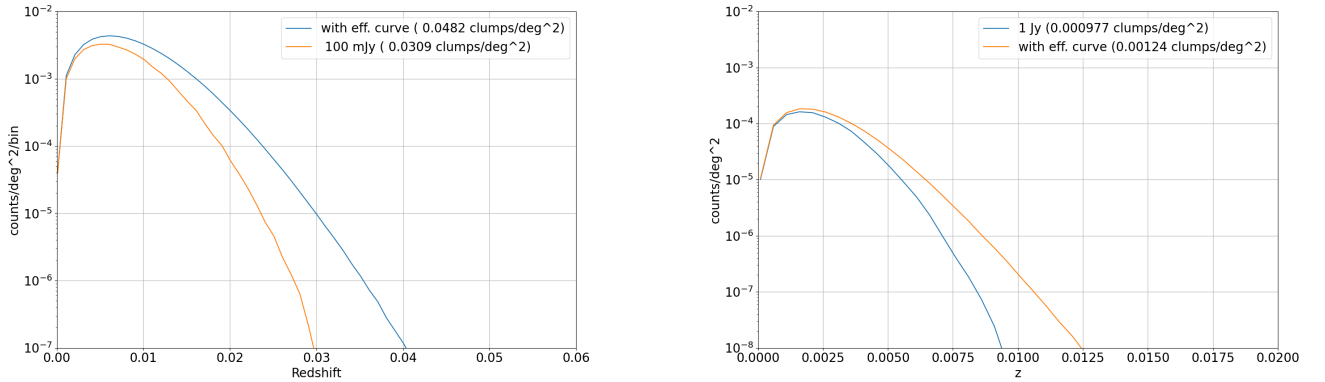


Figure 11. Expected number of detections vs redshift for the NCP (left-) and mid-latitude (right hand side) cases. The integral numbers of detections are reported in the caption of the figures. In both cases we indicate the results we obtain with a detection threshold on the flux, in Jy, and with the efficiency curves shown on figure 4.1.

survey. We begin by outlining the path from the galaxy parameters as recorded in the optical catalogs to their expected radio parameters. We then turn to the most straightforward case, extracting the cross-correlation between a Tianlai mid-latitude low redshift survey and the SDSS catalog, which overlaps its sky footprint. For the NCP case, the SDSS catalog does not cover this area.

We are in the process to construct a spectroscopic catalog based on the NCCS catalog (Gorbikov & Brosch 2014), and we will try to use this catalog to forecast its cross-correlation with Tianlai observations towards NCP. To complement this study, we also built an artificial catalog by rotating the coordinates from the SDSS catalog to get an overlap with observations towards NCP. This catalog would consist in a more complete catalog than the current state of the NCCS. The respective footprints of the SDSS and NCCS are shown on figure 5.

5.1 From optical photometry to radio parameters

In order to be able to simulate observations of a sky composed of diffuse and point-like continuum sources and an optical (of IR) galaxy 3D catalog we have to estimate the radio properties of the latter. We follow a two step procedure to achieve this. First, following Taylor et al. (2011) we estimate the stellar mass of each galaxy from their photometric properties using their equation 8 :

$$\log(M_*/M_\odot) = -0.68 + 0.70(M_g - M_i) - 0.4M_i \quad (19)$$

This equation can easily be applied for SDSS objects, using their Photoz table that includes absolute magnitudes. From a cross-match between the ALFALFA and SDSS, Brown et al. (2015) investigated the relation between the HI and stellar masses of galaxies. From their figure 3, where results of stacking ALFALFA observations for the full SDSS sample are reported, we extract a simple relation between the HI and stellar masses :

$$\log(M_{HI}/M_*) = 0.179 + 0.66(\log M_* - 9.21) \quad (20)$$

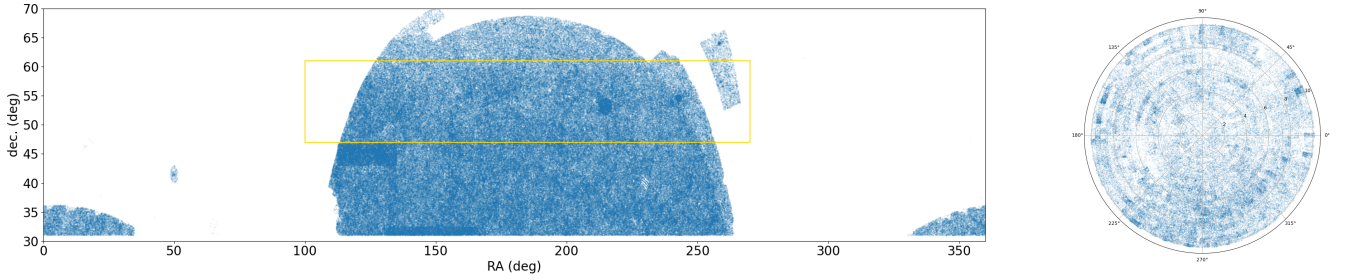


Figure 12. Footprints of the SDSS (left) and NCCS (right) catalogs used in this paper. We selected galaxies above $\delta = 30$ deg in the SDSS catalogs, and objects with PESS (point vs extended source identification) score greater than 2 in the NCCS. The rectangular area outlined on the SDSS footprint is the area where cross-correlation with Tianlai low- z simulated observations have been computed.

Combining equations 19 and 20 we can now estimate the HI mass for each galaxy. Moorman et al. (2014) (their figure 7) show the relation between the HI mass and 50% flux velocity dispersion (W50), from which we infer a simple linear relation between these two parameters.

Using equation this and 18 we finally can estimate the 21cm peak flux and frequency width for each galaxy, after accounting for their distance as determined by their redshift within a fiducial cosmology.

We prepared a catalog for our simulations from the SDSS photo- and spectroscopic catalog, selecting sources above $\delta = 30$ deg satisfying basic photometric parameters to select galaxies. Redshift and HI mass distribution of these sources are shown on figure 5.1.

The variations of their peak flux and frequency width is shown on figure

5.2 Mid-latitude survey cross-correlation with the SDSS catalog

To forecast the cross-correlation that could be reconstructed between Tianlai mid-latitude low- z observations, we have built a pipeline using several elements described in section 3.1 :

- (i) simulation of visibility that one observe with the T16DPA setup, combining signal and noise at sample level,
- (ii) reconstruction of sky maps with the m-mode approach, with pseudo-inverse
- (iii) filtering of these maps in harmonic space
- (iv) re-projection of the filtered maps in a equatorial band around the central latitude of the simulated observations, after foreground components removal using either of the two approaches presented in section 3.2
- (v) selection of the relevant portion of this band for cross-correlation studies, outlined in figure 5 (left hand side).

We ran this pipeline for two noise configurations to study systematic effects : with or without the 5 mK noise level on visibility samples. In this study, the HI sources are extrapolated from the SDSS catalogs as described in 5.1. The combined simulated signal could as in previous studies be one of the following combinations :

- (a) no signal (noise only simulation)
- (b) continuum sources only (Haslam-based synchrotron map and NVSS sources)

Bin	ν_{\min} (GHz)	$\nu_{\geq \delta, \gamma}$ (GHz)	z_{center}
1	1150	1200	0.173
2	1200	1240	0.141
3	1240	1280	0.113
4	1280	1320	0.085
5	1320	1360	0.057
6	1360	1400	0.029

Table 4. Frequency/redshift bins used from the mid-latitude Tianlai-SDSS cross-correlation analysis.

- (c) HI simulated sources only
- (d) the sum of all previous components

We ran this pipeline for all 1 MHz frequency planes between 1150 and 1400 MHz. For the evaluation of the cross-correlation of the resulting maps with the optical catalog, we compute for each analysed frequency interval a 'reference' plane from the sources positions (on the sky and in frequency using their redshift). Each plane consist in a rectangular map covering the analyzed sky area, with the same pixel size and area as the selected part of the reconstructed simulated map. Each pixel containing a source from the catalog with a frequency width overlapping that of the simulated map is set to unity. We then apply a 2D gaussian filter with a fixed width to this reference plane to roughly account for the (simulated) observations angular resolution. In addition to these 'reference planes' we also build 'null reference planes' following exactly the same procedure after randomizing the initial sources sky coordinates.

Finally, as explained in section 3 we compute auto- and cross C_ℓ for the reconstructed map portions and reference planes at each frequency. To get a more synthetic view we average these datasets over frequency we defined six frequency (or redshift) intervals described in table 4.

We present on figure 15 examples of auto-correlation power spectra we obtain after such averaging over frequencies from bin 5, without visibility noise. The spectrum prior to foreground subtraction seems to be truncated below $\ell \sim 100$ and above $\ell \gtrsim 750$, mainly as a result of the map-making and filtering procedure as shown in section 3.1. In between these two ℓ values, the effect of the foreground subtraction (polynomial fit) decreases the auto-spectrum by 3 to 4 orders. For comparison we also show the variations of the power spectrum from the 'reference plane'.

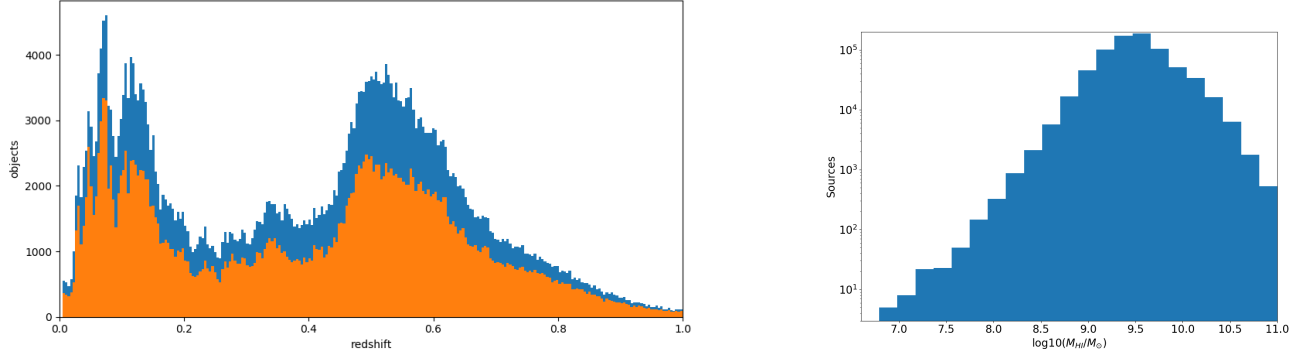


Figure 13. Redshift (left) and HI Mass (extrapolated from optical photometry) distributions from the SDSS catalog sources use in our simulations. The orange distribution correspond to our final source selection.

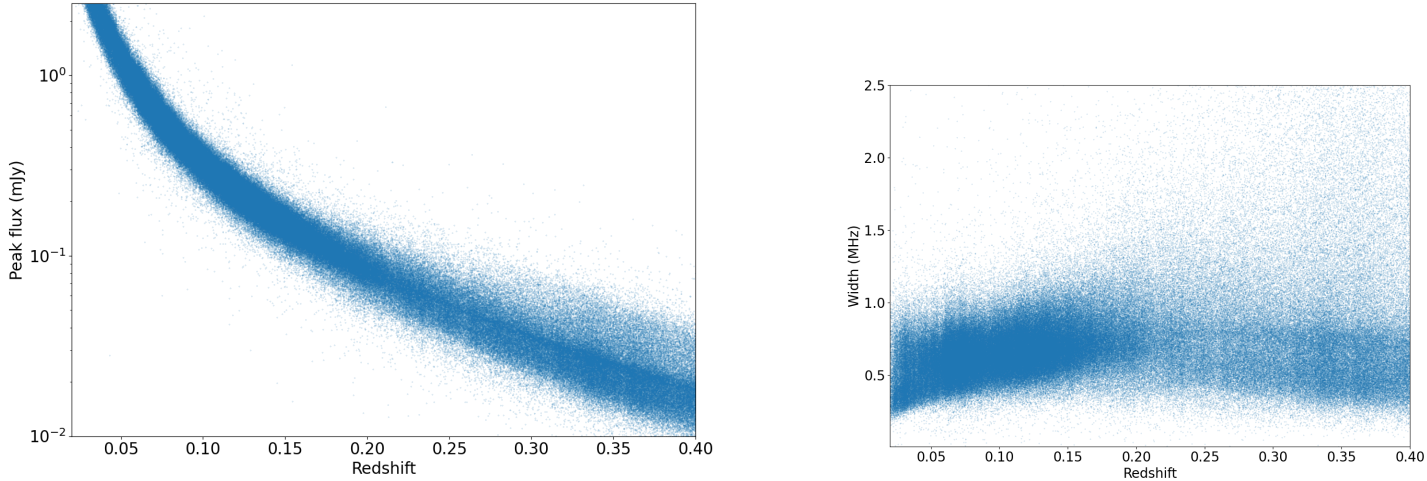


Figure 14. 21 cm flux and frequency width as a function of redshift for our simulated HI source set extrapolated from the SDSS catalogs.

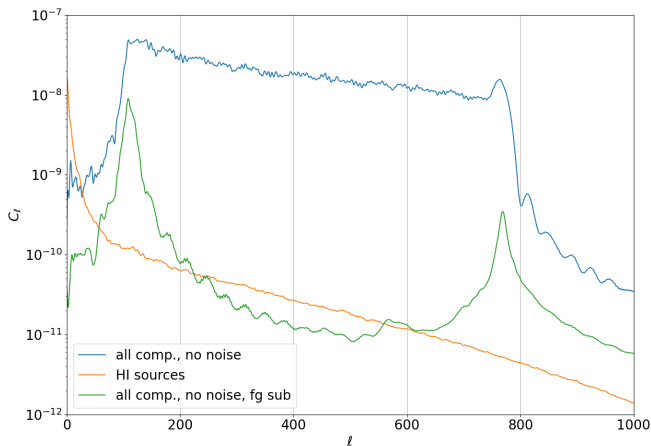


Figure 15. Average of auto-spectra coefficients (C_ℓ) from frequency bin 5. Blue and green curves correspond to the data with all components, with no noise added on visibilities, before (blue) and after (green) foreground subtraction (using polynomial fit in frequency domain). The orange curve is the auto-spectrum from the corresponding 'reference plane'

From the same frequency bin, we present in figure 16 averaged cross-power spectra between the 'reference plane' and data for the same cases : no visibility noise, all astrophysical components with and without foreground subtraction (blue and orange, respectively). The improvement brought by the foreground subtraction for extracting a non zero cross-correlation signal is evident. In that case, the cross-power spectrum amplitudes are indeed much decreased but stay above 0 for a broad range of multipoles, in the interval less perturbed by our map-making and filtering procedure. The same stays true, at least on average, in the presence of simulated noise at visibility level (green curve), showing that a significant cross-correlation signal could be extracted from a future Tianlai mid-latitude low- z survey.

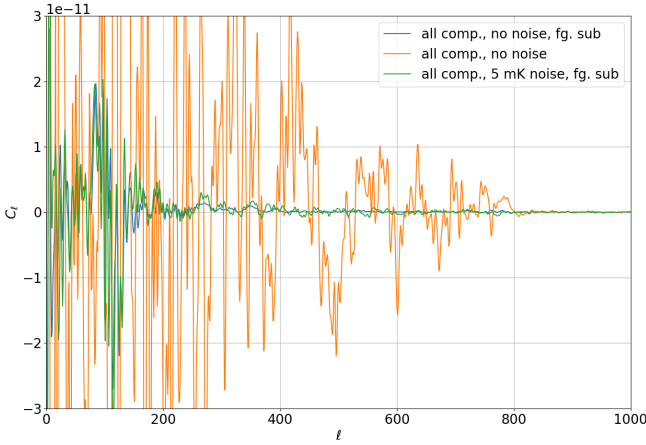


Figure 16. Average of cross-spectra coefficients (C_ℓ) from frequency bin 5. The orange and blue curve represent the cross-spectrum obtained between the ‘reference plane’ and data simulated with all astrophysical components but no noise, respectively before (orange) and after (blue) foreground subtraction (polynomial fit). The green curve shows the result obtained with 5 mK noise added, after foreground subtraction.

To get a more synthetic view of the cross-correlation detection perspective, we compute the average of the cross-spectra amplitudes for $\ell \in [250, 600]$, well within the ℓ range unperturbed by our map-making and filtering procedures. We present results of this averaging procedure for all redshift bins on figure 17. We compare the results with the two foreground subtraction methods (in blue and red) with two approaches of null test: we cross-correlate the ‘reference planes’ with simulated data without inclusion of HI sources of the corresponding catalog on the one hand (in black) and on the other hand, the simulated data are cross-correlated with the ‘null reference planes’.

From these results we can conclude that they do not show much dependence upon the foreground subtraction method applied. In both cases, we observe a positive cross-correlation between the SDSS catalog and Tianlai simulated data up to $z \sim 0.06$. This correlation is lower in the first redshift bin, mostly due to the much lower number of sources at these very low z in SDSS. This positive correlation does not show up in the two ‘null tests’ we also analysed: using simulations w/o SDSS-derived HI sources on the one hand, and shuffling the reference planes on the other hand.

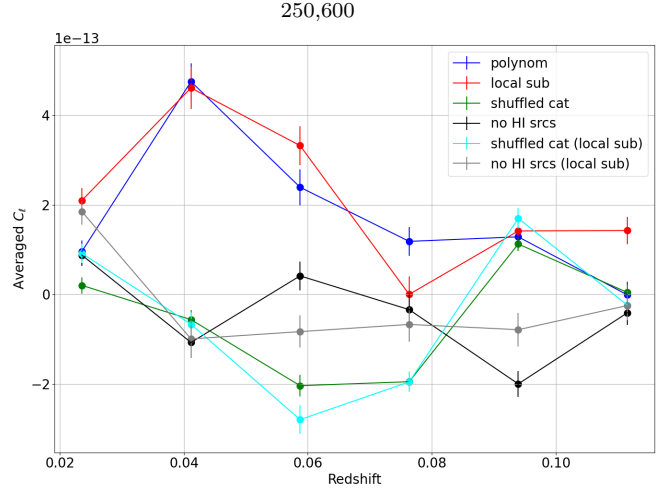


Figure 17. Average of the cross-correlation C_ℓ in the interval $\ell \in [250, 600]$ for each of the redshift bins defined in table 4, for the two component separation techniques applied on the full simulation or simulation omitting HI sources cross-correlated to the ‘reference planes’ or ‘null reference planes’.

5.3 Cross-correlation towards NCP

5.3.1 With a rotated SDSS catalog

5.3.2 With NCCS

6 DISCUSSION

Discussion / Optimal strategy: NCP area coverage and redshift ranges, mid-latitude coverage and redshift ranges

Is there anything to say about direct detection at redshift about 0.4

ACKNOWLEDGEMENTS

This research made use of Photutils, an Astropy package for detection and photometry of astronomical sources (Bradley et al. (2021)).

REFERENCES

- Ansari R., et al., 2012, *A&A*, **540**, A129
 Ansari R., et al., 2020, *MNRAS*, **493**, 2965
 Baldwin J. E., Boysen R. C., Hales S. E. G., Jennings J. E., Waggett P. C., Warner P. J., Wilson D. M. A., 1985, *MNRAS*, **217**, 717
 Bandura K., et al., 2014, in Stepp L. M., Gilmozzi R., Hall H. J., eds, Society of Photo-Optical Instrumentation Engineers (SPIE) Conference Series Vol. 9145, Ground-based and Airborne Telescopes V. p. 914522 ([arXiv:1406.2288](https://arxiv.org/abs/1406.2288)), [doi:10.1117/12.2054950](https://doi.org/10.1117/12.2054950)
 Battye R. A., Davies R. D., Weller J., 2004, *MNRAS*, **355**, 1339
 Bharadwaj S., Nath B. B., Sethi S. K., 2001, *Journal of Astrophysics and Astronomy*, **22**, 21
 Bradley L., et al., 2021, astropy/photutils: 1.2.0, [doi:10.5281/zenodo.5525286](https://doi.org/10.5281/zenodo.5525286), <https://doi.org/10.5281/zenodo.5525286>

- Brown T., Catinella B., Cortese L., Kilborn V., Haynes M. P., Giovanelli R., 2015, *Monthly Notices of the Royal Astronomical Society*, 452, 2479–2489
- Bull P., Ferreira P. G., Patel P., Santos M. G., 2015, *ApJ*, 803, 21
- Chang T.-C., Pen U.-L., Peterson J. B., McDonald P., 2008, *Phys. Rev. Lett.*, 100, 091303
- Chen X., 2012, in *International Journal of Modern Physics Conference Series*. pp 256–263 ([arXiv:1212.6278](#)), [doi:10.1142/S2010194512006459](#)
- Condon J. J., Cotton W. D., Greisen E. W., Yin Q. F., Perley R. A., Taylor G. B., Broderick J. J., 1998, *AJ*, 115, 1693
- Cosmic Visions 21 cm Collaboration et al., 2018, arXiv e-prints, p. [arXiv:1810.09572](#)
- Das S., et al., 2018, in Zmuidzinas J., Gao J.-R., eds, *Society of Photo-Optical Instrumentation Engineers (SPIE) Conference Series Vol. 10708, Millimeter, Submillimeter, and Far-Infrared Detectors and Instrumentation for Astronomy IX*. p. 1070836 ([arXiv:1806.04698](#)), [doi:10.1117/12.2313031](#)
- Gorbikova E., Brosch N., 2014, *Mon. Not. Roy. Astron. Soc.*, 443, 725
- Haslam C. G. T., Klein U., Salter C. J., Stoffel H., Wilson W. E., Cleary M. N., Cooke D. J., Thomasson P., 1981, *A&A*, 100, 209
- Hogg D. W., 1999, arXiv e-prints, pp [astro-ph/9905116](#)
- Jones M. G., Haynes M. P., Giovanelli R., Moorman C., 2018, *Monthly Notices of the Royal Astronomical Society*, 477, 2–17
- Li J., et al., 2020, *Science China Physics, Mechanics, and Astronomy*, 63, 129862
- Moorman C. M., Vogeley M. S., Hoyle F., Pan D. C., Haynes M. P., Giovanelli R., 2014, *Monthly Notices of the Royal Astronomical Society*, 444, 3559–3570
- Morales M. F., Wyithe J. S. B., 2010, *ARA&A*, 48, 127
- Newburgh L., et al., 2016, in *Ground-based and Airborne Telescopes VI*. p. 99065X
- O’Connor P., et al., 2020, in *Society of Photo-Optical Instrumentation Engineers (SPIE) Conference Series*. p. 114457C ([arXiv:2011.08695](#)), [doi:10.1117/12.2576250](#)
- Pritchard J. R., Loeb A., 2008, *Phys. Rev. D*, 78, 103511
- Remazeilles M., Dickinson C., Banday A. J., Bigot-Sazy M. A., Ghosh T., 2015, *MNRAS*, 451, 4311
- Seo H.-J., Dodelson S., Marriner J., McGinnis D., Stebbins A., Stoughton C., Vallinotto A., 2010, *ApJ*, 721, 164
- Shaw J. R., Sigurdson K., Sitwell M., Stebbins A., Pen U.-L., 2015, *Phys. Rev.*, D91, 083514
- Smoot G. F., Debono I., 2017, *A&A*, 597, A136
- Taylor E. N., et al., 2011, *Monthly Notices of the Royal Astronomical Society*, 418, 1587–1620
- The CHIME/FRB Collaboration et al., 2021, arXiv e-prints, p. [arXiv:2106.04352](#)
- Vanderlinde K., et al., 2019, in *Canadian Long Range Plan for Astronomy and Astrophysics White Papers*. p. 28 ([arXiv:1911.01777](#)), [doi:10.5281/zenodo.3765414](#)
- Villaescusa-Navarro F., Alonso D., Viel M., 2017, *MNRAS*, 466, 2736
- Wu F., et al., 2021, *MNRAS*, 506, 3455
- Zhang J., Ansari R., Chen X., Campagne J.-E., Magneville C., Wu F., 2016, *MNRAS*, 461, 1950

This paper has been typeset from a $\text{\TeX}/\text{\LaTeX}$ file prepared by the author.